

Extrusion temperature impacts on biometallic Mg-2.0Zn-0.5Zr-3.0Gd (wt%)

solid-solution alloy

Huai Yao^{a,b}, Jiuba Wen^{a,b,*}, Yi Xiong^{a,b}, Yan. Lu^a, Fengzhang Ren^{a,b}, Wei. Cao^{c,d}

^aSchool of Materials Science and Engineering, Henan University of Science and Technology,

Luoyang Henan 471023, China;

^b Collaborative InnovationCenter of Nonferrous Metals of HenanProvince, LuoyangHenan 471023,

China

^cNano and Molecular Systems Research Unit, University of Oulu, FIN-90014, Finland

^dSchool of Mechanical and Automotive Engineering, Anhui Polytechnic University, Wuhu 241000,

China

ABSTRACT:

To obtain ideal implant materials, we hot extruded Mg-2.0Zn-0.5Zr-3.0Gd solid-solution alloys, and studied extrusion temperature impacts on materials properties. Fine dynamic recrystallized (DRXed) grains (~5 μm) and elongated coarse un-dynamic recrystallized (unDRXed) deformed grains turned out at the range of 470-490 °C, but changed to bigger ones (~8 μm) and abnormal growth (30~40 μm) at 490-510 °C. Precipitated phases consist of rod-like (Mg, Zn)₃Gd particles and newly precipitated Mg₂Zn₁₁ rectangles. The alloy extruded at 490 °C meets all mechanical and anticorrosive requirements for biomaterials, thanks to evenly distributed second phases via the solid solution, and the grain refinements through the hot extrusion.

Keywords: Magnesium alloys; Microstructure; Mechanical properties; Corrosion; Extrusion

* corresponding author. J.B. Wen

E-mail address: wenjiuba12@163.com

1. Introduction

An ideal implant material should be equipped with proper mechanical properties and corrosion resistance, along with its biocompatibility. As a possible candidate, the magnesium (Mg) alloys have attracted considerable attentions for biomaterial applications due to their good biocompatibility and promising biodegradability [1-3]. However, some key problems including rapid corrosion rate, localized corrosion mode and low mechanical properties remain to be solved before their practical applications as biomaterials [4]. Grain refinement may work for property improvements. The refinement leads to a decrease in the corrosion resistance in an active environment, but results in an increase of corrosion resistance in an encouraging passive environment [5]. In the simulated human environments where inert reaction happens, reduction in grain size would encourage lower rates of uniform corrosion. In earlier works, Ralston and Birbilis suggested that the increased grain boundary density compensate oxide/base metal mismatch by decreasing compressive stress that otherwise would lead to cracks in the oxide film [6-7]. The magnesium alloy surfaces were covered with more stable oxide layer with finer grains, accounting for better anticorrosive performances.

Indeed, the Mg alloy refinements can be reached by typical thermo-mechanical processes such as hot rolling and hot extrusion. Corrosion resistances are improved in the hot rolled alloys [8-9]. It was reported that after rolling, the binary Mg alloys evolved less hydrogen and got lower corrosion rates when immersed in simulated body fluid (SBF) or Hank's solution [10]. Similar behavior has also been found in

hot-rolled Mg-X alloys (except for Mg0.1Zr and Mg0.3Si) [11]. Mechanical properties are enhanced with the method. An ultimate tensile strength (UTS) of 393 MPa, yield strength (YS) of 306 MPa and elongation to failure (EL) of 14.6% have been reached in the Mg-8.2Gd-3.8Y-1.0Zn-0.4Zr (wt %) alloy [12], and the numbers turn to 418 MPa, 330 MPa and 7.5% in the Mg-3Gd-1Zn-0.2Zr (at %) alloy [13]. Hot rolling the as-cast Mg-Gd-Zn-Zr-Mn alloy resulted in an elongation of 21.3% along with the low corrosion rate <0.5 mm/year [14]. On the other hand, hot extrusion was also applied to refine microstructures and improve mechanical properties of Mg alloys [15-18]. The extraordinary 542 MPa UTS and 473 MPa YS were reported for the Mg-10Gd-5.7Y-1.5Zn-0.65Zr with the method [19-20]. The mechanisms are in general attributed to more homogeneous microstructure, but smaller second-phase particles in the fine-grained alloys after the thermotreatments [21].

Despite improvements in mechanical and anticorrosive aspects, the aforementioned methods suffer from a drawback that the second phases cannot be completely dissolved nor precipitated in the alloys through these thermoprocesses [22]. These phases have banding distributions along the extrusion direction (ED), introducing uncertainties to mechanical properties and corrosion resistances of the alloys [23]. A prior solid-solution processing to the extrusion precursor may help to wipe these barrels. Advantage stems from the fact that a large number of second phases have been solved into alloy matrices before being extruded. Thanks to the solid solution, the second phases in alloys may re-precipitate nanoscale second phase particles in the process of extrusion, distributing homogeneously in alloy matrix.

In this paper, we reported on extrusion temperature (T_E) impacts on morphological, mechanical, and chemical properties of the solid-solution Mg alloys. Thanks to joint effects of the solid solution and hot extrusion, the maximum UTS of 249(3) MPa, YS of 228(3) MPa, and EL of 29.8(0.8)% are reached when $T_E=490$ °C. The sample also has low corrosion rates less than 0.5 mm/y in weight loss and hydrogen evolution tests, and a uniform corrosion behavior. To the best of our knowledge, it is the first time to employ hot extrusion for the post-treatment of the solid-solution Mg alloys. Besides realizing a facile route to process the implanting Mg metal alloy, the physical mechanisms beyond unique materials functionality are also revealed. Although the as-extruded sample needs further clinical tests before practical applications, the superior properties make the alloy a promising candidate as a graft material for the bones.

2. Experimental

2.1 Sample preparation

Alloy ingot with a nominal composition of Mg-2.0Zn-0.5Zr-3.0Gd alloy (wt%) was prepared in an electronic induction furnace under the $\text{CO}_2+2\%\text{SF}_6$ mixed gas protection. The high purity Mg (purity $\geq 99.93\%$), Zn (purity $\geq 99.93\%$), and Mg-25Zr (wt%) and Mg-20Gd (wt%) master alloys were used as raw precursors. The melt was cast into a preheated mild steel mold of 160 mm \times 45 mm \times 100 mm in size. The actual chemical composition of as-cast alloy was found to be Mg-1.95Zn-0.44Zr-2.84Gd (wt.%) after analysis using an inductively coupled plasma atomic emission spectrometry (Optima 8000).

The cast ingots were homogenized at 480 °C for 8 hours, followed by quenching into water at about 60 °C. They were then machined into blocks with the size of $\Phi 50$ mm \times 35 mm for extrusion. The extrusion die was preheated to 300 °C. The cylindrical ingots were preheated at different T_E of 470, 480, 490, 500, 510 °C for 2 hours. Hereafter, these as-extruded samples are denoted as E470, E480, E490, E500, E510, respectively. They were hot extruded into rods with a diameter of 18 mm at an extrusion ratio of ~ 8 , and a speed of 5 mm/s. The extruded rods were cooled to room temperature in the air. All the extruded rods were carried out with relief annealing at 200 °C for 4 hours. Six individual samples were extruded at each T_E .

2.2 Microstructure determination and mechanical properties test

The specimens for microstructure measurements were cut parallel to the ED, mechanically polished, and etched with acid solutions (5 mL picric acid, 5 mL acetic acid, 100 mL absolute ethyl alcohol and 10 mL distilled water). The microstructures were characterized using optical microscopy (OLYMPUS) and scanning electronic microscopy (SEM). Transmission electron microscopy (TEM) was carried out using a JEM-2010 at 200 kV. The TEM samples were machined by wire-cutting the extruded rods parallel to the ED. Thin foils for TEM observation were punched into discs of 3 mm in diameter, mechanically polished to about 70 μ m, and then twin-jet electropolished in a solution of 97% ethyl alcohol and 3% perchloric acid at -45 °C and 0.1 A. At last a twin-gun precision ion polishing system (Gatan, model 691) was used for ion milling at last. The extruded rods were machined into tensile specimens of 5 mm gauge diameter and 25 mm gauge length parallel to the ED. Tensile tests

were performed at room temperature by using a AG-1250KN (SHIMADZU) machine at a tensile speed of 1 mm/min.

2.3 Electrochemical corrosion test

Potentiodynamic polarization and electrochemical impedance spectroscopy (EIS) were carried out to evaluate the corrosion behavior of Mg-2.0Zn-0.5Zr-3.0Gd alloys in SBF at 37 °C on an electrochemical workstation (Autolab PGSTAT128N). The SBF has the following composition: 8.0 g/L NaCl, 0.14 g/L CaCl, 0.4 g/L KCl, 0.35 g/L NaHCO₃, 0.1 g/L MgCl₂·6H₂O, 1.0 g/L Glucose, 0.06 g/L Na₂HPO₄·12H₂O, 0.06 g/L KH₂PO₄, and 0.06 g/L MgSO₄·7H₂O [24-26].

The three-electrode configuration was adopted in the electrochemical test. The alloys with a surface area of $\Phi 11.3 \text{ mm} \times 10 \text{ mm}$ were used as working electrode, a saturated calomel electrode as reference electrode, and a graphite sheet as counter electrode. The working electrodes were connected to a copper wire and then embedded in the epoxy resin. The mounted samples were mechanically polished and exposed with a surface area of 1 cm². In order to keep stability of the experiment, the potentiodynamic polarization and EIS measurements were carried out after soaking the working electrodes in SBF for 1 hour. Potentiodynamic polarization testing was performed from -0.25 V in the cathodic direction to +0.4 V in the anodic direction based on the open circuit potential at a scan rate of 1 mVs⁻¹. EIS measurements were performed at open circuit potential (OCP) with AC amplitude of 10 mV and a frequency range from 0.1 Hz to 10 kHz in SBF.

2.4 Immersion corrosion test

The simplest measurement of the corrosion rate is the weight loss rate test by immersion experiment in SBF. The loss ΔW (mg) can be translated to an average corrosion rate, P_w (mm/y) using

$$P_w = 87.6 \Delta W / \rho A t \quad [1]$$

Here P_w is corrosion rate measured by weight loss, ρ the alloys density (g/cm³), A the specimen surface area (cm²), and t the immersion time (hour) [27]. The samples with diameters of 18 mm and thicknesses of 5 mm were immersed into 180 mL solutions whose temperatures were maintained at 37 °C with a water bath. The immersion test lasted for 120 hours and the immersion solution was renewed every 8 hours in order to keep the pH stable.

The corrosion rate of alloys was also evaluated in SBF by hydrogen evolution experiment. The sample with a dimension of $\Phi 18$ mm \times 5 mm was horizontally immersed in 180 mL SBF. The SBF was kept in a beaker open to air. The hydrogen evolved during the corrosion experiment was collected in a burette above the corroding sample. The amount of hydrogen can be measuring from the height difference of the SBF in the measuring burette [28-29]. Samples were immersed in SBF for up to 120 hours at 37 °C. The total volume of evolved hydrogen gas was recorded when immersion solution was renewed every 8 hours in order to achieve a better simulation result. The hydrogen evolution rate, V_H (mL) was evaluated by dividing the evolved hydrogen volume by the time of evolution. The hydrogen evolution rate, V_H , was converted to corrosion rate [30], P_H (mm/y) using:

$$P_H = 95.36 V_H / \rho A t \quad [2]$$

3. Results

3.1 Microstructure

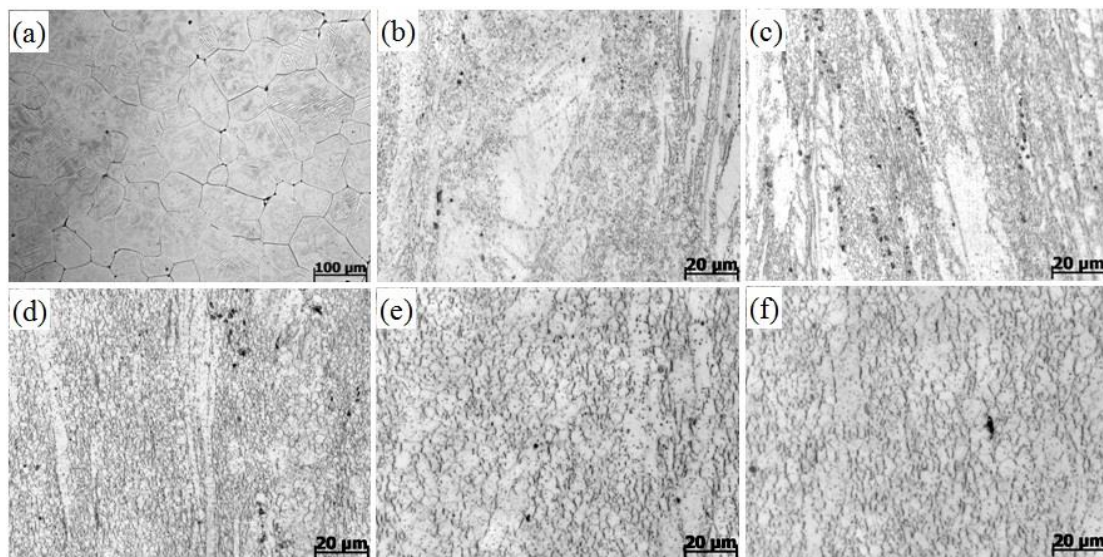


Fig. 1. The optical images of the Mg-2.0Zn-0.5Zr-3.0Gd alloys: (a) solution treated; (b) E470; (c) E480; (d) E490; (e) E500; (f) E510.

Fig. 1 shows the optical micrographs of solid solution treated and extruded alloy on longitudinal section along the ED. As shown in Fig. 1(a), the solid solution alloy has an uniform grain structure, and the initial average grain size is about 150 μm. Fig. 1(b)-(f) shows the optical micrographs of the extruded Mg-2.0Zn-0.5Zr-3.0Gd alloy at various T_{ES} . Compared with the microstructure of solid solution alloy, the grain size of as-extruded alloys was remarkably refined, indicating that the dynamic recrystallization occurred at these temperatures. In the range from 470 to 490 °C, the as-extruded alloys show bimodal-grained microstructures along the ED, containing both fine DRXed grains (5 μm) and elongated coarse unDRXed deformed grains. In general, the area fraction of DRXed increases with T_E at 470-490 °C range. The DRXed microstructure tops ~95% total area and has a size of ~5.0 μm. Dynamic recrystallization has almost completely taken place at 490 °C. The DRXed grains

further grew with the T_E . From 500 to 510 °C, both normal and abnormal growths happened to part of the DRXed grains. The sizes of the normal and abnormal grains are about 8 μm and 30~40 μm , respectively.

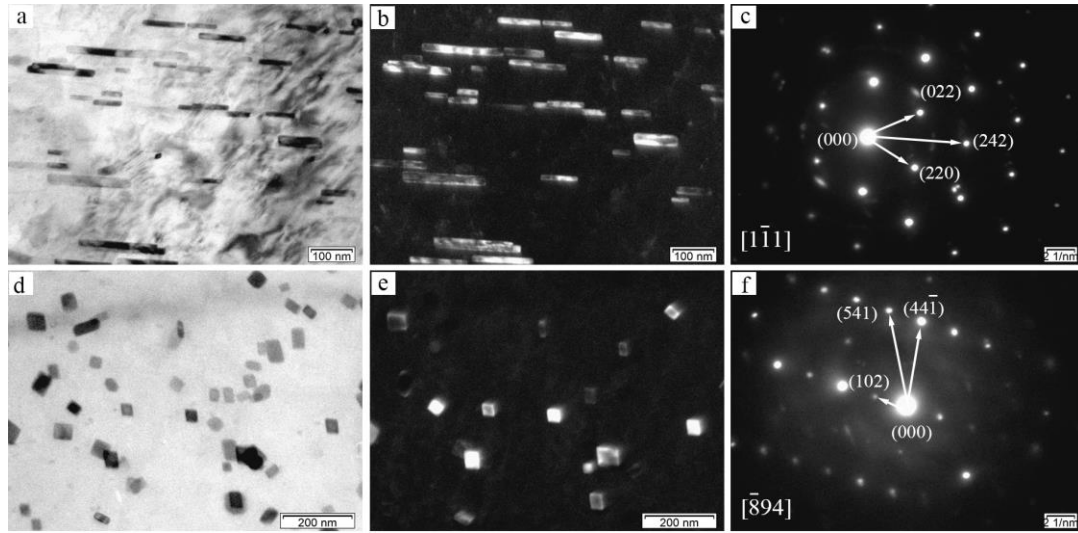


Fig. 2. Microstructure of the E490 alloy: (a) and (b) are bright field and dark field micrographs of the rod-like precipitates; (c) corresponding SAED pattern of (a) and (b) with incident electron beam // $[1\bar{1}1]$; (d) and (e) are bright field and dark field micrographs of the rectangle shape precipitates; (f) corresponding SAED pattern of (d) and (e) with incident electron beam // $[\bar{8}94]$.

The TEM micrographs of the E490 alloy are shown in Fig. 2. The bright field image shows densely dispersed rod-like particles with 100-400 nm length and 20-40 nm width (Fig. 2(a)). Rod-like particles are oriented along the ED in the dark field image in Fig. 2(b). According to the corresponding selected area electron diffraction (SAED) pattern (Fig. 2(c)), the rod-like precipitated phase has a face-centered cubic (fcc) structure. The interplanar spacing of SAED pattern in Fig. 2(c) are 0.2507 nm, 0.2507 nm and 0.1443 nm, respectively, indexed to (220), (022), and (242) planes of the Mg_3Gd . A lattice constant $a=0.7084$ nm is observed along the $[1\bar{1}1]$ zone axis. In analogy to the Mg_3Gd phase ($a=0.7324$ nm), it was identified to $(\text{Mg}, \text{Zn})_3\text{Gd}$ phase where Zn is dissolved in the structure, in accordance with results for other alloys

[31-32]. It is worth noting that the cohesive energy of (Mg, Zn)₃Gd phase was much lower than the corresponding value of Mg₃Gd phase, suggesting a more stable (Mg, Zn)₃Gd phase than the Mg₃Gd counterpart. Compared to the Mg₃Gd phase with positive enthalpy, the (Mg, Zn)₃Gd phase has negative formation enthalpy, resulting in a stronger alloying ability [33].

In addition, some of nanoscale particles were observed distributing within α -Mg matrix, as shown in Fig. 2(d) and (e). The rectangle particles are smaller than 50 nm. According to the SAED pattern shown in Fig. 2(f), the particles have a primitive cubic lattice structure. The interplanar spacing of SAED pattern in Fig. 2(f) is determined to 0.3842 nm, 0.1492 nm and 0.1321 nm, respectively, indexed to the (102), $(44\bar{1})$ and (541) planes of the Mg₂Zn₁₁. A lattice constant $a=0.8574$ nm is found along the zone axis, and identified from the $[\bar{8}94]$ plane of the Mg₂Zn₁₁ (Mg₂Zn₁₁, PDF65-1853, Pm-3, $a=0.8552$ nm). However, no other phase was detected apart from the α -Mg matrix, the rod-like, and rectangle nanoparticles in the E490.

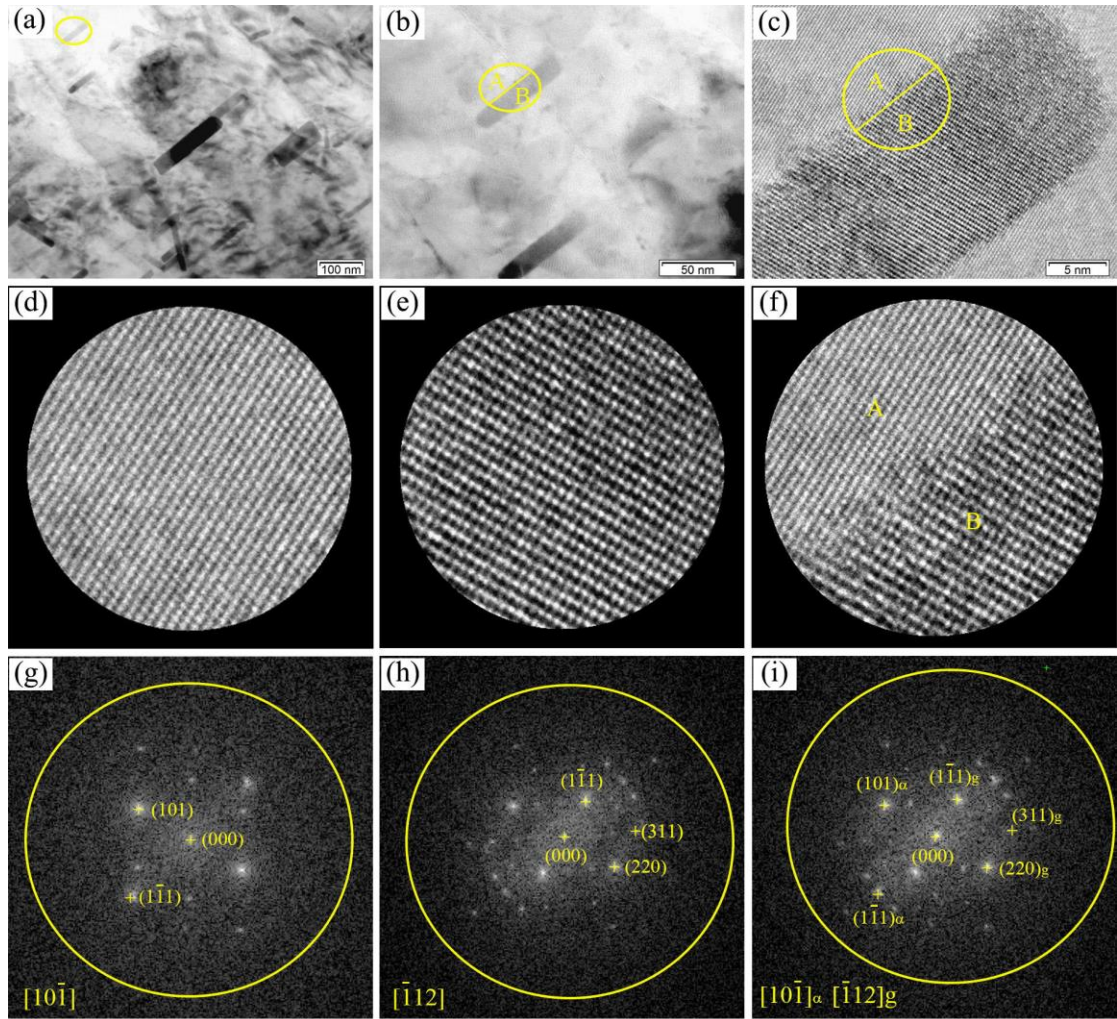


Fig. 3. TEM images of E490 alloy: (a) and (b) Bright field image of E490 alloy; (c) HRTEM image of E490 alloy; (d) HRTEM image of the α -Mg matrix; (e) HRTEM image of the rod-like precipitated phase; (f) HRTEM image of the α -Mg matrix and rod-like precipitated phase; (g) FFT image of (d); (h) FFT image of (e); (i) FFT image of (f).

Fig. 3(a)-(b) depict TEM images of the E490 alloy. Apparently, rod-like precipitated phase is oriented along the ED in α -Mg matrix. In Fig. 3(c) a high resolution transmission electron microscope (HRTEM) image shows a clear interfacial boundary between the rod-like precipitated phase and the matrix, with each sides zoomed in Fig. 3(d) and (e). By the fast Fourier transforms (FFT) of HRTEM micrograph shown in Fig. 3(g), the matrix phase marked at A place was identified as α -Mg with electron beam // $[10\bar{1}]_{\alpha}$. The rod-like precipitated phase at B was identified

as $(\text{Mg, Zn})_3\text{Gd}$ phase with their axis parallel to $[\bar{1}12]_g$ direction according to the corresponding FFT image shown in Fig. 3(h). An amplified HRTEM image of the interface is shown in Fig. 3(f), with its FFT in Fig. 3(i). The interplanar spacing of $(101)_a$ and $(220)_g$ were around 0.2452 nm and 0.247 nm. These results indicate that $(\text{Mg, Zn})_3\text{Gd}$ phase has a coherent interface relationship with $\alpha\text{-Mg}$ matrix.

Based on above evidences, we also studied the origins of the rod-like phases. As illustrated in Fig. 3(a)-(i), these nanorods tended to dynamically precipitate rather than the original second phase breakage during the extrusion process, suggesting dissolution of pre-existing $(\text{Mg, Zn})_3\text{Gd}$ phase under high deformation temperature. Some rod-like particles distributed dispersedly in the $\alpha\text{-Mg}$ matrix when extrusion temperature was about 490 °C, indicating that dynamic precipitation also occurred during extrusion at appropriate deformation temperature. Hence, the rode-like precipitated phase originates from the $\alpha\text{-Mg}$ matrix.

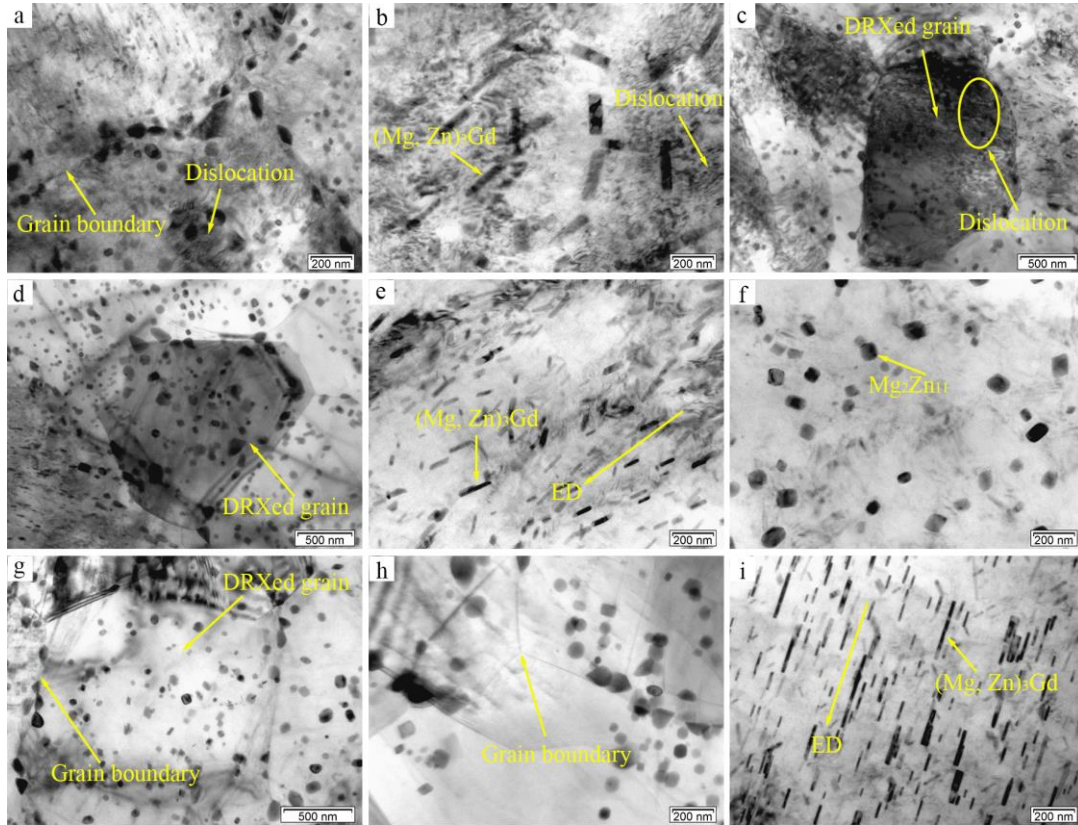


Fig. 4. Typical TEM bright-field images of the Mg-2.0Zn-0.5Zr-3.0Gd alloys at different extrusion temperature: (a) and (b) E470; (c) E480; (d), (e) and (f) E490; (g) E500; (h) and (i) E510.

The temperature dependent morphologies were investigated through TEM bright-field images as shown in Fig. 4 for the precipitated phases, dislocations and their distributions in the alloys extruded at 470 °C in (a) and (b), 480 °C in (c), 490 °C in (d)-(f), 500 °C in (g), and 510 °C in (h) and (i). Some nanoscale rod-like and rectangle shape particles distributed dispersedly in the matrix when the extrusion temperature was in the 470-510 °C range. They are clearly seen in Fig. 4(a)-(b) where a large amount of nanoparticles are distributed along grain boundaries (GBs) (indicated by yellow arrow in Fig. 4(a)) in the E470 alloy. Besides, these structures largely existed within both elongated coarse unDRXed grains and DRXed grains. The size of the nanoparticles was about 20-100 nm. A large amount of rod-like particles

with diameter of 20-50 nm and 200-400 nm in length were dispersed within in grains and oriented along the ED. A mass of accumulated dislocations could be observed inside alloy matrix. When temperature increased to 480 °C, high density dislocations were observed in the DRXed grain region (Fig. 4(c)). Moreover, the fine DRXed grains are around 4.5 μm in size, rectangle in shape, and associated with nano-scaled precipitators at the GBs and within the grains. Once at the boundaries, these particles (20-40 nm in size) strongly inhibited the growth of DRXed grains.

However, when the extrusion temperature was increased to 490 °C, the dislocation density in alloy matrix was remarkably reduced as seen in Fig. 4(d)-(f). Compared with E480, the size of the DRXed grains and rectangle shape particles had little change in E490. The rod-like particles have the diameter of 5-10 nm and length of 50-200 nm. Their amount was reduced, but uniformly distributed along the ED in E490 alloy. When extruded at 500 °C, the E500 owns normally growing DRXed grains. The rectangle shape particles precipitated mainly along the DRXed GBs and only existed in the DRXed zone (Fig. 4(g)). A small amount of dislocations were near the grain boundaries. After being extruded at 510 °C, the fine rectangle shape particles were dynamically precipitated at the grain boundaries and within the grain interiors (Fig. 4(h)). In the region containing abnormal growing grains (Fig. 4(i)), high density rod-like particles with diameter of 20-50 nm and 200-400 nm in length were observed in the abnormal growing grain region and distributed along the ED.

3.2 Mechanical properties

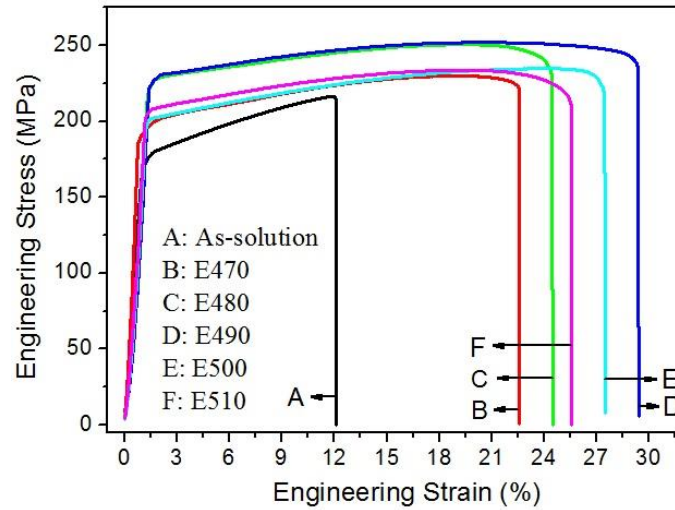


Fig. 5. Engineering stress-strain curves at room temperature of the solution-heat-treated and hot extrusion alloys.

Table 1 Mechanical properties of the solution-heat-treated and hot extrusion alloys

$E_t(^{\circ}\text{C})$	As-solution	470	480	490	500	510
UTS (MPa)	213 ± 3	229 ± 3	247 ± 3	249 ± 3	223 ± 3	227 ± 3
YS (MPa)	172 ± 3	203 ± 3	227 ± 3	228 ± 3	197 ± 3	202 ± 3
EL (%)	12.5 ± 0.6	22.9 ± 0.8	24.7 ± 0.9	29.8 ± 0.8	26.8 ± 0.9	24.5 ± 0.8

The engineering stress-strain curves of the solution-heat-treated and E470-510 alloys tested at room temperature are shown in Fig. 5. The UTS, YS, and EL are tabulated in table 1 for alloys extruded at different temperatures together with their solid solution precursor. Obviously, the alloy without hot extrusion possess rather low mechanical properties. As for the extruded ones, in general, the UTS, YS and EL of the as-extruded alloys increase with deformation temperature within the 470-490 $^{\circ}\text{C}$ range. However, at 490 $^{\circ}\text{C}$ to 510 $^{\circ}\text{C}$ range, these parameters decrease. Mechanical properties follow the DRXed fractions as the result of extrusion temperature. The alloy extruded at 490 $^{\circ}\text{C}$ owns the highest UTS of 249 ± 3 MPa, YS of 228 ± 3 MPa and EL of $29.8\pm0.8\%$. Mechanical properties of the E490 alloy fully meet medical requirements [34].

3.3 Fracture characteristics

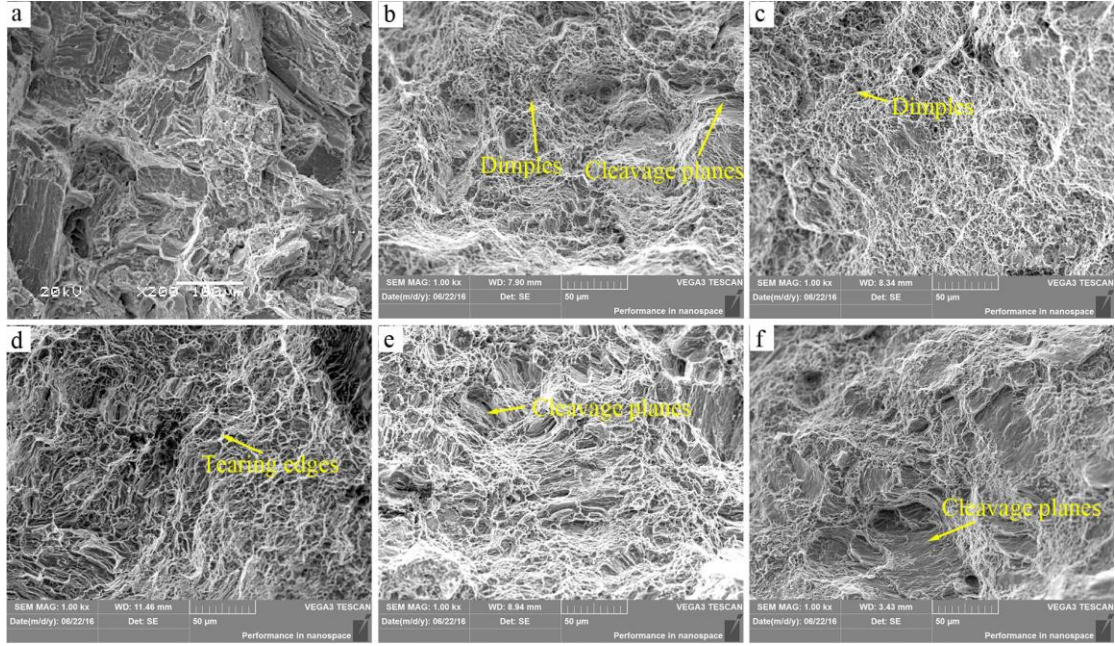


Fig. 6. SEM images of fracture surfaces of solid solution and as-extruded alloys: (a) As-solution; (b) E470; (c) E480; (d) E490; (e) E500; (f) E510.

Fig. 6 shows SEM fracture morphologies of the solid solution sample and these extruded at different T_{ES} . Without further thermo treatment, cleavage fracture dominants in the alloys as Fig. 6(a) shows. The structures of the fracture surface and failure mode are quite similar for E470-510 alloys. The fracture surfaces are mainly consisted of a large number of small dimples and tearing edges with the features of plastic fracture. Such dimples are similar to these in a previous work for the extruded Mg-4Zn-1Y alloys [35].

As shown in Fig. 6(b)-(f), when T_E stayed at 470-490 °C range, distributions of the plastic dimples become wider and more uniform among the tearing edges. However, at the 500-510 °C range, while the semi-cleavage planes on the fracture surfaces increase gradually with the temperature, the plastic dimples decrease obviously.

3.4 Polarization tests

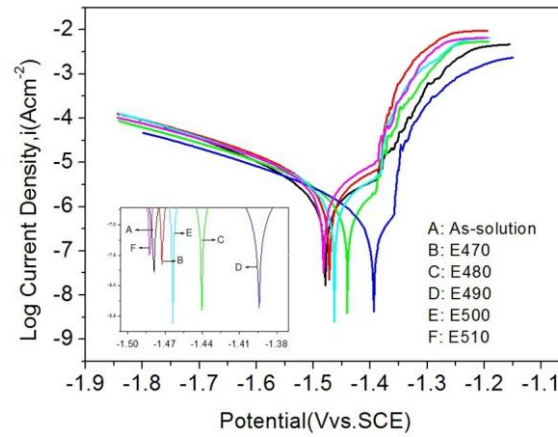


Fig. 7. Potentiodynamic polarization curves of the alloys after immersion in SBF for 1 hour.

Table 2 Values measured from potentiodynamic and corrosion rate of the alloys

Material	As-solution	E470	E480	E490	E500	E510
E_{Corr} (V vs. SCE)	-1.480	-1.470	-1.440	-1.393	-1.462	-1.481
I_{Corr} (μAcm^{-2})	4.042	3.630	3.364	2.575	3.588	4.057
P_i (mm/y)	0.183	0.164	0.152	0.116	0.163	0.183

Fig. 7 presents the polarization curves measured after 1 hour in SBF at 37 °C for the solution-heat-treated and extruded alloys. Samples have similar polarization curve shapes in the solution. The free corrosion potentials (E_{corr}), free corrosion current densities (I_{corr}) and free corrosion rate (P_i) values evaluated from polarization curves are listed in table 2. The cathodic polarization curves represent the cathodic hydrogen evolution, and the anodic polarization curves represent the dissolution of Mg.

The solution-heat-treated alloys have more negative E_{corr} , high I_{corr} and P_i . The E_{corr} gradually shifts to the positive direction, and I_{corr} and P_i continuously decreases for samples extruded at the temperature range of 470 to 490 °C. Such trends turn to opposite within the range of 490 to 510 °C. The E_{corr} , I_{corr} and P_i of the E490 alloy are -1.393 V vs. SCE, 2.575 μAcm^{-2} and 0.116 mm/y, respectively. These parameters indicate that the extrusion temperature had a considerable effect on the corrosion rate of the solution-heat-treated alloy. The high E_{corr} together with a high corrosion

resistance and low I_{corr} clearly demonstrate a lower P_i of the E490 alloy.

3.5 Immersion tests

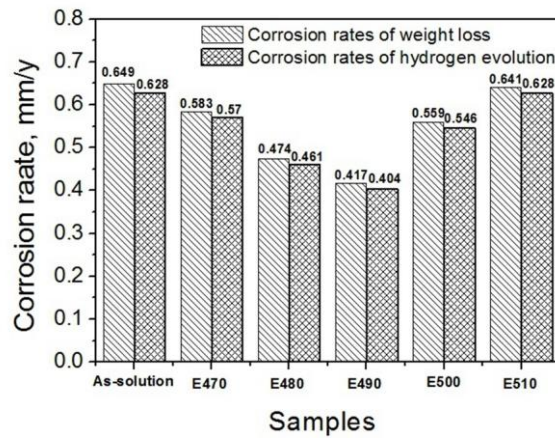


Fig. 8. Corrosion rates for solution-heat-treated and hot extrusion alloys measured by weight loss and hydrogen evolution after immersed for 120 hours.

Fig. 8 shows the corrosion rates for solution-heat-treated and hot extrusion alloys measured by weight loss and hydrogen evolution for the duration of 120 hours. The corrosion rates from hydrogen evolutions are systematically lower than these from weight loss. This is not surprising. During the immersions, the emitted hydrogen can be dissolved in the SBF or Mg metal, while a certain amount of second phase particles may be dropped out or removed together with the corrosion products [11]. The corrosion rates gradually decrease following the temperature rises from 470 to 490 °C, and then increase from 490 to 510 °C. Minimum corrosion rates of the E490 alloy were determined to 0.417 mm/y and 0.404 mm/y respectively in weight loss and hydrogen evolution methods. The E490 is a good candidate for medical implanting alloys [34].

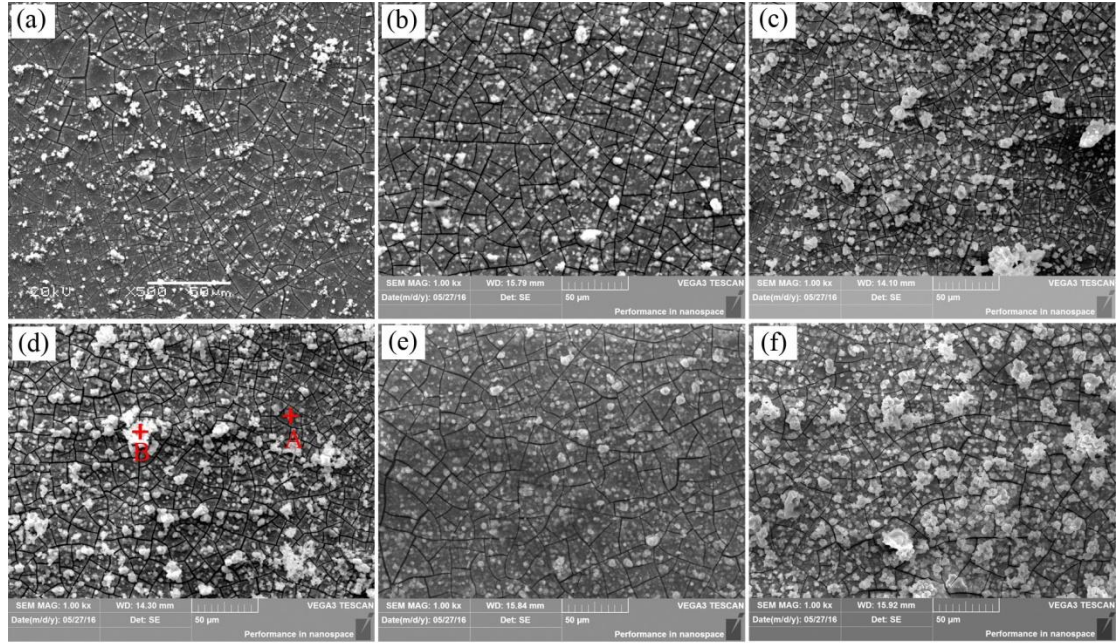


Fig. 9. Corrosion micrographs of the Mg-2.0Zn-0.5Zr-3.0Gd alloys after immersion in SBF for 120 hours: (a) As-solution; (b) E470; (c) E480; (d) E490; (e) E500; (f) E510.

Table 3 EDS results of the E490alloy after immersion in SBF for 120 hours (wt.%)

Position	O	Mg	P	Ca	Na
A	48.53	4.37	16.38	30.72	0
B	49.17	4.73	16.44	27.71	1.75

Fig.9 shows the surface morphologies of the Mg-2.0Zn-0.5Zr-3.0Gd alloys immersed in SBF for 120 hours. It can be seen that the magnesium samples were covered by rather uniform films decorated with bright particles distributed all over the corrosion layer. As showed in Fig. 9(a)-(f), many cracks are on the surface, due to the dehydration of the corrosion products after being dried in warm air [36]. EDS test results corresponding to the areas marked by A and B in Fig. 9(d) are analyzed and the results are shown in table 3. The main elements of the corrosion products are identified as O, Mg, P, Ca and Na elements. At the A place in Fig. 9(d), the products are rich in Ca but do not contain Na. The presence of Na in the corrosion products is most probably due to inadequate washing.

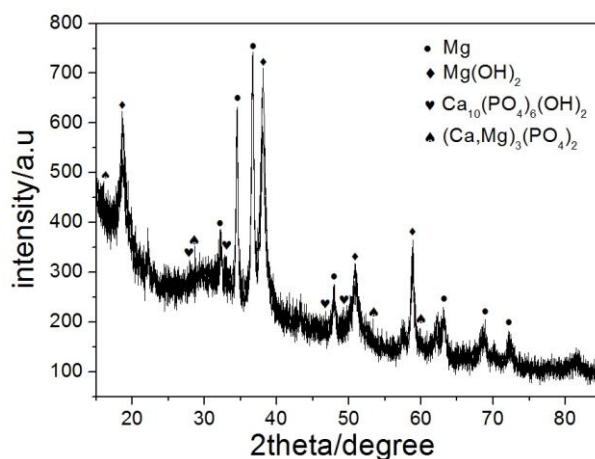


Fig. 10. X-ray diffraction patterns of the corrosion products of E360 alloy after immersion in SBF for 120 hours.

Fig. 10 illustrates further XRD patterns of E490 after immersing in SBF for 120 hours. The magnesium hydroxide $[\text{Mg}(\text{OH})_2]$ is the dominant products for the samples immersed in SBF. However, the calcium magnesium phosphate $[(\text{Ca}, \text{Mg})_3(\text{PO}_4)_2]$ and hydroxyapatite $[\text{Ca}_{10}(\text{PO}_4)_6(\text{OH})_2]$ are also found in the corrosion products for the samples exposed in SBF. Furthermore, $(\text{Ca}, \text{Mg})_3(\text{PO}_4)_2$ has similar chemical compositions as the natural bone, yet owning good biocompatibility and osteoconductivity [37]. The deposition of $\text{Ca}_{10}(\text{PO}_4)_6(\text{OH})_2$ particles during immersion accelerate the recovery of bone tissue [38]. Thus, present Mg alloys have good biocompatibility.

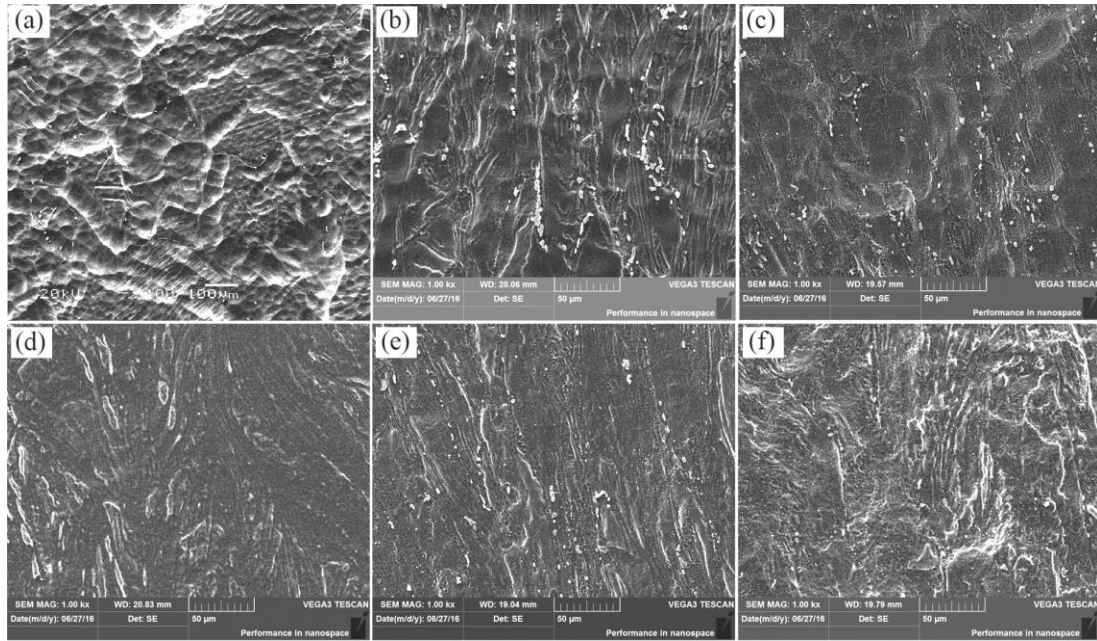


Fig. 11. SEM micrographs showing the corroded samples after immersion for 120 hours and corrosion product removal. (a) As-solution; (b) E470; (c) E480; (d) E490; (e) E500; (f) E510.

Fig.11 presents the corroded surface after 120 hours immersion in SBF and after corrosion product removal. The whole surface was corroded and wrinkled as shown in Fig. 11(a). In addition, there were some small holes and second phase particles on the corrosion surface. This alloy suffered from the most serious corrosion among all the alloys. The formation of coarse surfaces is mainly attributed to the uneven existence of alloying elements in the matrix. The existence of small holes indicates the micro-galvanic corrosion due to discontinuity of the second phases in the solution-heat-treated conditions and occurrences of serious localized corrosions. The residual second phase in the solid solution process acts as the cathode, which not only accelerates the anodic dissolution rate but also leads to the localized corrosion of the matrix adjacent to it by galvanic corrosion. The detachment of the second phase left formations of corrosive pores.

Fig. 11(b) and (c) present the corroded surfaces after immersion test for E470

alloy and E480 alloy. The whole surface was corroded with some small shallow areas, and few second phase particles oriented along the ED in the matrix. The existence of small shallows may be attributed to the elongated coarse unDRXed deformed grains (as shown in Fig. (1)). Fig. 11(d) presents the corroded surfaces after the immersion test for E490 alloy. There was relatively uniform corrosion over the whole surfaces, but also some original areas suffering from little corrosion. Fig. 11(e)-(f) presents the corroded surface after the immersion test for E500 alloy and E510 alloy. The E510 alloy suffered from the most serious corrosion among all the extruded alloys. A large amount of normally growing DRXed grains and a small quantity of abnormal growing grains in the E510 alloy matrix might cause potential difference. This easily leads to galvanic corrosion, which further accelerates the corrosion rate. Additionally, the abnormal growing grains themselves have low corrosion resistance [5].

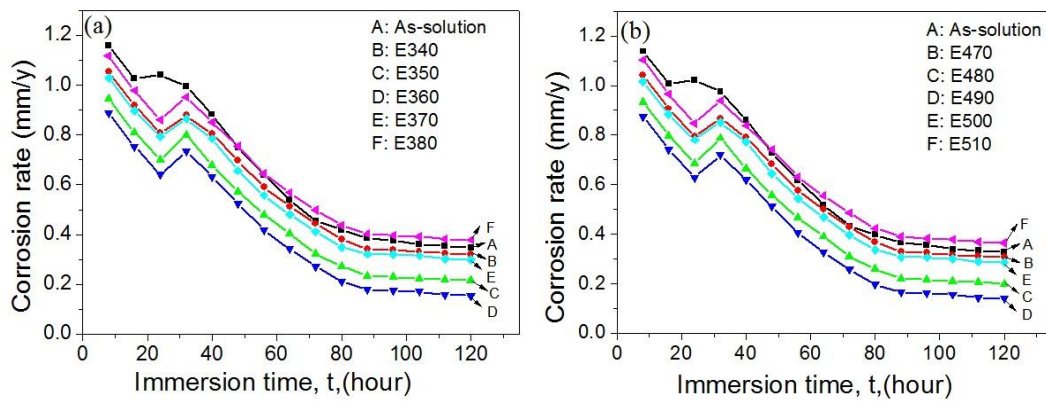


Fig. 12. Corrosion rates for alloy measured by weight loss and hydrogen evolution every 8 hours: (a) Corrosion rates of weight loss; (b) Corrosion rates of hydrogen evolution.

The time courses of the corrosion rate variation are depicted in Fig. 12(a) and (b) for solution-heat-treated and hot extrusion alloys measured by weight loss and

hydrogen evolution, respectively. Similar trends are found in corrosion rates measured through both methods. For solution-heat-treated Mg-2.0Zn-0.5Zr-3.0Gd alloy, the corrosion rate gradually decreases during the first 16 hours of immersion, then increases within the 16-24 hours range, and then decreases but stabilizes after 96 hours. For hot extrusion alloys, each of the steps is delayed by 8 hours of immersion. This result indicates that there was an incubation period of low corrosion rate, followed by an acceleration of the corrosion rate to a steady state value. Compared with the solution-heat-treated Mg-2.0Zn-0.5Zr-3.0Gd alloy, the hot extrusion alloys have a longer incubation period. Large variation in microstructures and the second phases lead to inconsistent change trend of corrosion rate within the first 24 hours. This trend is also showed in Ref. [39] with as-cast and solution-heat-treated Mg₆₇-Zn₂₈-Ca₅ alloys at the initial stage of immersion.

3.6 EIS measurements

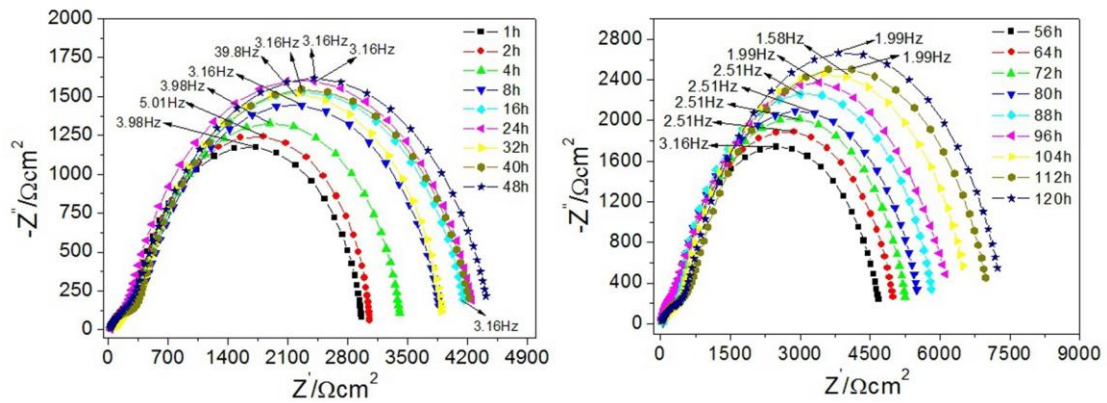


Fig. 13. Nyquist plots of E490 alloy after immersion in SBF for different time.

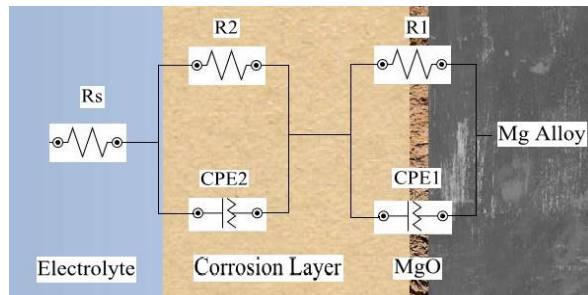


Fig. 14. Equivalent electrical circuit (EEC) used to fit the EIS data obtained on E490 alloy in SBF.

Table 4 Fitting parameters for E490 alloy in SBF after different immersion time

Time (hour)	Z'	-Z''	R _S R(Ω)	R _{P1} R(Ω)	CPE Y ₀₁ (Um ho)	CPE N	R _{P2} R(KΩ)	CPE Y ₀₂ (Um ho)	CPE N
1	2965	1173	13.7	330	22.6	0.597	2.64	18.3	0.921
2	3061	1234	13.8	389	24.4	0.602	2.66	13.3	0.958
4	3407	1329	19.1	412	40.3	0.543	3.02	18.0	0.919
8	3869	1443	24.3	420	39.5	0.502	3.46	19.6	0.884
16	4157	1532	18.0	410	15.1	0.599	3.89	20.4	0.854
24	4251	1599	26.3	418	9.8	0.731	3.96	17.9	0.847
32	3899	1502	72.6	359	27.2	0.559	3.49	14.9	0.905
40	4214	1544	14.2	404	10.8	0.605	3.86	21.0	0.849
48	4419	1614	16.8	419	24.0	0.596	4.05	19.8	0.840
56	4684	1741	35.7	421	9.6	0.708	4.32	18.4	0.838
64	4997	1888	17.4	423	10.4	0.686	4.63	18.2	0.857
72	5250	2018	20.8	433	17.2	0.603	4.87	17.2	0.875
80	5588	2094	43.4	435	37.7	0.577	5.13	18.8	0.851
88	5817	2263	24.8	441	37.7	0.569	5.45	17.4	0.871
96	6114	2372	23.2	456	35.1	0.541	5.64	21.1	0.861
104	6494	2454	11.1	492	30.2	0.512	5.79	23.7	0.852
112	6977	2503	7.1	530	10.1	0.594	5.99	17.1	0.839
120	7235	2664	6.3	554	12.4	0.581	6.07	18.6	0.838

Fig. 13 shows the impedance response of E490 alloy in SBF after different immersion times up to 120 hours. The diameters of the Nyquist plots gradually increase in the first 24 hours, decrease from 24 hours to 32 hours, and then continuously increase with immersion times up to 120 hours. Different corrosion stages can be tracked accordingly. The first increase in diameters is related to decreases of the corrosion rate thanks to the protective layer formation during the first 24 hours. Smaller diameters of the plots from 24 hours to 32 hours are attributed to the rupture of the corrosion layer and the presence of the fast localized corrosion process. After 32 hours, localized corrosion is weakened, while the corrosion layer becomes thick enough. The diameters become bigger.

In order to fully understand the corrosion process and investigate the time

dependence of the E490 alloy corrosion mechanisms, a two-time constant electrical equivalent circuit (EEC) was used to fit the impedance response (Fig. 14). The capacitive loop in the higher frequency region is attributed to the charge transfer resistance, while at lower frequency region is associated with the diffusion of ions transport in the solid phase through the corrosion layer. In this equivalent circuit, the R_s is represent solution resistance between the reference electrode and the sample. The CPE_1 and R_{p1} describe, respectively, the capacitance at the substrate/MgO film corrosion layer and the charge transfer resistance through MgO barrier film. The R_{p2} describes the resistance of Mg^{2+} through the outer corrosion layer, and CPE_2 is the corresponding capacitance at corrosion layer/electrolyte interface [40]. Constant phase elements (CPE) are employed instead of pure capacitances because of the non-ideal double layer capacitive response. The impedance value of a CPE is

$$\text{calculated by [41]: } Z_{CPE} = \frac{1}{Y_0(j\omega)^n} \quad (3)$$

where Y_0 is the CPE constant, ω the angular frequency. n is the CPE dimensionless exponent, denoting deviation from the ideal capacitive behavior ($0 < n \leq 1$). If n is equal to 1, CPE is identical to that of a capacitor.

Table 4 shows the EIS fitting parameters for E490 alloy obtained after different immersion times. The parameter of R_s has a value about $20 \Omega \text{ cm}^{-2}$ in SBF. The sum of R_{p1} and R_{p2} increase slowly with immersion times during the first 24 hours, suggesting probably initial formation of a porous $Mg(OH)_2$ /carbonated corrosion layer. The layer became thicker as a result of corrosion resistance increase and corrosion layer porosity decrease. Between 24 hours and 32 hours, the R_{p1} increases slowly with

immersion times, which can be related to increase protective inner MgO layer thickness in most of the area. Decrease of R_{p2} can be attributed to the rupture of the corrosion layer at the grain boundary where vigorous hydrogen was emitted in localized corrosion and corrosion layer was dissolved after adsorption of chloride ions. After 32 hours, the R_{p2} slightly rises and then gradually tends to be stable up to 120 hours. This is attributed to the dissolution and generation of corrosion products close to the dynamic equilibrium state. The R_{p1} has a smaller change in the vicinity of $400 \Omega\text{cm}^{-2}$ and no regularity, probably due to the dynamic fluctuation on formation and dissolution of a protective inner $\text{Mg}(\text{OH})_2$ corrosion products. The sum of R_{p1} and R_{p2} slowly increased with the prolongation of immersion time and approached to the stabilized value after 104 hours. The reaction tends to be stable, forming more compact corrosion products layer on the alloy surface.

4. Discussion

Fig. 1(b)-(f) show the optical micrographs of the hot extrusion alloys. Compared with the microstructure of solution-heat-treated alloy (Fig. 1(a)), the grain size of hot extrusion alloys was remarkably refined, indicating that the DRXed occurs in E470-510 alloys. The deformation temperature dominates the DRXed processes in solid solution $\text{Mg-2.0Zn-0.5Zr-3.0Gd}$ alloy when the extrusion ratio was about 8. In terms of microstructure evolution within the 470-490 °C range (Fig. 4), dislocation density in DRXed and unDRXed grain regions decreases drastically with extrusion temperature. In general, recrystallization kinetics increases with extrusion temperature [42]. Both the grain size and distribution strongly depend on the extrusion

temperature [43]. As shown in Fig. 4, the E480-490 alloys have smaller grains with an average diameter of 5.0 μm because growth during extrusion was inhibited due to presence of a certain amount of precipitates. This smaller grain size was yet another indication for the existence of dynamic precipitates at 490 °C, which suggests that these dynamic precipitates be effective in suppressing the grain growth during hot extrusion, resulting in the refinement of DRXed grains. This pinning effect of particles would be much influential during extrusion at 480-490 °C. Many studies have been dedicated to the use of second-phase particles to control the microstructure and mechanical properties through DRX in alloys [42, 44]. The pinning effect is weakened when extrusion temperature was higher than 500 °C. The grain boundaries were pinned by small particles after a higher deformation temperature, and dislocations were continuously trapped into these grain boundaries, eventually leading to their transformation into high angle grain boundaries [45].

The cleavage planes and tearing ridges dominant, which is typical of brittle fracture, can be observed on the tensile fracture surface of the solution-heat-treated alloy (Fig. 6(a)). Rather large grains exist within the matrix, resulting in the poor mechanical properties. The structures of the fracture surface and failure mode are quite similar for as-extruded alloys. The main differences in mechanical properties of the as-extruded alloys are due to their different DRXed fraction and grain size. At room temperature, the basal dislocation is attributed to the dominant deformation mechanism. The fine-grained structure has good mechanical properties according to the Hall-Petch relation [46]. Besides the grain boundary strengthening, second phase

strengthening is also an important factor in the present study. As shown in Figs. 2 and 4, large amount of rod-like and rectangle precipitates were formed during extrusion process. They act as barriers to dislocate motions and increase the stresses. The alloy extruded at 490 °C showed better comprehensive mechanical properties compared with other four alloys (Table 1). This is mainly attributed to the fine uniform dispersed precipitates and fine DRXed grains as well as relatively high DRXed fraction. The excellent ductility of the extrusion alloys is mainly ascribed to the following factors: (1) The fine DRXed grains contribute to the activation of non-basal slip systems which can obviously enhance the ductility and strength of the alloy [47]. (2) Due to the coherences of the rod-like precipitated phase with the α -Mg matrix, the precipitated rods formed after hot extrusion contribute to the excellent plasticity and high strength. (3) The weakened recrystallization basal texture facilitates the basal slip, which can also improve the ductility and strength [48]. As shown in Fig. 6(d), these dimples are obviously larger and deeper when the extrusion temperature was about 490 °C. Such a fracture surface indicates that the good ductility of wrought magnesium alloys can be obtained when the extrusion temperature is about 490 °C.

Discrepancies are noticed between the corrosion rates given by the corrosion current at the free corrosion potential and by the direct measurements using weight loss [49]. The free corrosion typically starts from a localized corrosion after an incubation and slowly expands over the sample surface [50]. Thus, the P_i from the Tafel extrapolation interprets the onset of corrosion. In contrast, the rate from the weight loss measurement is yielded from corrosions averaged over a considerable

period (120 hours), most of which is counted after the corrosion onset [51]. Therefore, the corrosion rates differ in the short-term tests (P_i) and long-term tests (P_w). Despite of the small discrepancy, the trend of corrosion rates by using weight loss and hydrogen evolution is in good agreement with the results estimated by Tafel extrapolation (Table 2).

Recent literatures suggest that corrosion behavior of Mg and its alloys can be significantly altered by grain refinement and researchers have reported improvement in corrosion resistance of Mg and its alloys [52-53]. Thus, we study morphological influences on the corrosion behavior of the extruded solid solution alloys. The high fraction of fine grain in the microstructures helps to reduce corrosion rates in the following four ways: Firstly, the discontinuity of the crystal structures between MgO and Mg substrate leads the development of high compressive stress within the oxide layer on coarse-grained Mg alloys. One way to reduce the structural discontinuity and lower disorders between MgO and matrix surface is to introduce large volume fraction of grain boundaries by grain refining. As a result, the higher area fraction of DRXed per unit volume in Mg alloys reduces degrees of the MgO layer cracking. The $Mg(OH)_2$, typically formed at the outside of MgO, can bring disturbances in the film and likely cause compressive rupture of the surface layer. The initial MgO layer formed on the fine-grained magnesium alloy provides better surface coverage, and provides a means to inhibit subsequent rupture of exterior $Mg(OH)_2$ layer [54]. This would improve the corrosion resistance of Mg alloys. Secondly, the higher area fraction of DRXed microstructure leads to lower dislocation density in the

microstructure, consequentially decelerating corrosions. Thirdly, the grain boundary acts as a physical corrosion barrier, and a smaller grain size is in favor of the corrosion resistance [8]. Fourthly, the Gd addition to Mg-2.0Zn-0.5Zr alloy in general improves the anticorrosion response of the alloy. This is attributed to the increase corrosion potential of the Gd metal, and a protective layer formed by it after being solidly solved to the magnesium matrix.

The higher area fraction of DRXed microstructure for E490 alloy was likely to reduce propensity of localized corrosion attack and yield uniform corrosion in three ways. Firstly, fine grain will lead to formation of closely spaced electrochemical batteries of anodic and cathodic regions, which led to more uniform attack. Secondly, the fined microstructure with lower gradient of electrochemical potential within the matrix have more homogeneous microstructures. Thirdly, the nanoscale second phase particles are distributed more homogeneously in the matrix.

5. Conclusions

In conclusion, we systematically studied the effects of extrusion temperature on the microstructure, mechanical properties and corrosion resistance of solid-solution Mg-2.0Zn-0.5Zr-3.0Gd alloys. Possible mechanisms were also proposed. The main conclusions are as follows.

1. The E470-490 alloys show bimodal-grained microstructures along the ED, containing both fine DRXed grains (5 μm) and elongated coarse unDRXed deformed grains. The area fraction of DRXed microstructure increases with T_E at 470 to 490 $^{\circ}\text{C}$. The maximum area fraction of DRXed microstructure of E490 alloy is estimated

to 95%. In the range of 500 to 510 °C, it is consisted of the normal growth of the DRXed grains (~8 μm) and the abnormal growth (30~40 μm) grains.

2. The precipitated phases of extruded alloys are composed of nanoscale rod-like (Mg, Zn)₃Gd grains parallel to the ED and nanoscale rectangle shape Mg₂Zn₁₁ phase. The rectangle shape Mg₂Zn₁₁ precipitated phase is a new precipitated phase in the extrusion process. The rode-like (Mg, Zn)₃Gd precipitated phase originates from the α-Mg matrix.

3.The UTS, YS and EL of the as-extruded alloys increase with the T_{ES} within the 470-490 °C range, and then decreases when was tuned within 490 and 510 °C. The maximum UTS, YS and EL at room temperature of E490 alloy are 249±3 MPa, 228±3 MPa and 29.8±0.8%, respectively.

4. The corrosion rates of the E490 alloy, calculated by weight loss and hydrogen evolution immersing in SBF at 37 °C for 120 hours, are both less than 0.5 mm/y. In addition, the E490 alloy showed a uniform corrosion. The lowest corrosion rate and uniform corrosion characteristic of the E490 alloy may relate to its refinement microstructure.

Acknowledgements

This work was supported by the Henan new nonferrous metal materials University Science and technology innovation team support program of china (2012IRTSTHN008),the Program for Science, Technology Innovation Talents in Universities of the Henan Province (17HASTIT026), the Science and Technology Project of the Henan Province (152102210077), Education Department of the Henan

Province (16A430005) and the Science and Technology Innovation Team of the Henan University of Science and Technology (2015XTD006). W. Cao acknowledges financial supports from Oulu University Strategic Grant. W. Cao thanks financial supports from Center for Advanced Steel Research (CASR), University of Oulu.

References

- [1] B. Homayun, A. Afshar, Microstructure, mechanical properties, corrosion behavior and cytotoxicity of Mg-Zn-Al-Ca alloys as biodegradable materials, *J. Alloys. Comp.* 607 (2014) 1-10.
- [2] L. Mao, H. Zhou, L. Chen, J.L. Niu, L. Zhang, G.Y. Yuan, C.L. Song, Enhanced biocompatibility and long-term durability in vivo of Mg-Nd-Zn-Zr alloy for vascular stent application, *J. Alloys. Comp.* 720 (2017) 245-253.
- [3] L. Yang, Y. Huang, F. Feyerabend, R. Willumeit, C. Mendis, K.U. Kainer, N. Hort, Microstructure, mechanical and corrosion properties of Mg-Dy-Gd-Zr alloys for medical applications, *Acta Biomater.* 9 (2013) 8499-8508.
- [4] X.B. Zhang, Y.J. Wu, Y.J. Xue, Z.Z. Wang, L. Yang, Biocorrosion behavior and cytotoxicity of a Mg-Gd-Zn-Zr alloy with long period stacking ordered structure, *Mater. Lett.* 86 (2012) 42-45.
- [5] S. Gollapudi, Grain size distribution effects on the corrosion behaviour of materials, *Corros. Sci.* 62 (2012) 90-94.
- [6] K.D. Ralston, N. Birbilis, Effect of grain size on Corrosion: A Review, *Corrosion.* 66 (2010) 319-324.
- [7] D. Orlov, K.D. Ralston, N. Birbilis, Y. Estrin, Enhanced corrosion resistance of

- Mg alloy ZK60 after processing by integrated extrusion and equal channel angular pressing, *Acta Mater.* 59 (2011) 6176-6186.
- [8] N.N. Aung, W. Zhou, Effect of grain size and twins on the corrosion behavior of AZ31B magnesium alloy, *Corros. Sci.* 52 (2010) 589-594.
- [9] J.W. Seong, W.J. Kim, Development of biodegradable Mg-Ca alloy sheets with enhanced strength and corrosion properties through the refinement and uniform dispersion of the Mg_2Ca phase by high-ratio differential speed rolling, *Acta Biomater.* 11 (2015) 531-542.
- [10] X. Gu, Y. Zheng, Y. Cheng, S. Zhong, T. Xi, In vitro corrosion and biocompatibility of binary magnesium alloys, *Biomaterials*, 30 (2009) 484-498.
- [11] F.Y. Cao, Z.M. Shi, G.L. Song, M. Liu, M.S. Dargusch, A. Atrens, Influence of hot rolling on the corrosion behavior of several Mg-X alloys, *Corros. Sci.* 90 (2015) 176-191.
- [12] C. Xu, M.Y. Zheng, K. Wu, E.D. Wang, G.H. Fan, S.W. Xu, S. Kamado, X.D. Liu, G.J. Wang, X.J. Lv, M.J. Li, Y.T. Liu, Effect of final rolling reduction on the microstructure and mechanical properties of Mg-Gd-Y-Zn-Zr alloy sheets, *Mater. Sci. Eng. A* 559 (2013) 232-240.
- [13] J.S. Zhang, W.B. Zhang, L.P. Bian, W.L. Cheng, X.F. Niu, C.X. Xu, S.J. Wu, Study of Mg-Gd-Zn-Zr alloys with long period stacking ordered structures, *Mater. Sci. Eng. A* 585 (2013) 268-276.
- [14] Z.Z. Gui, Z.X. Kang, Y.Y. Li, Mechanical and corrosion properties of Mg-Gd-Zn-Zr-Mn biodegradable alloy by hot extrusion, *J. Alloys. Comp.* 685

- (2016) 222-230.
- [15] Z.W. Yu, A.T. Tang, Q. Wang, Z.Y. Gao, J.J. He, J. She, K. Song, F.S. Pan, High strength and superior ductility of an ultra-fine grained magnesium-manganese alloy, *Mater. Sci. Eng. A* 648 (2015) 202-207.
- [16] S.M. Baek, J.S. Kang, H.J. Shin, C.D. Yim, B.S. You, H.Y. Ha, S.S. Park, Role of alloyed Y in improving the corrosion resistance of extruded Mg-Al-Ca-based alloy, *Corros. Sci.* 118 (2017) 227-232.
- [17] Y. Yan, H.W. Cao, Y.J. Kang, K. Yu, T. Xiao, J. Luo, Y.W. Deng, H.J. Fang, H.Q. Xiong, Y.L. Dai, Effects of Zn concentration and heat treatment on the microstructure, mechanical properties and corrosion behavior of as-extruded Mg-Zn alloys produced by powder metallurgy, *J. Alloys. Comp.* 693 (2017) 1277-1289.
- [18] J. Geng, J.F. Nie, Microstructure and mechanical properties of extruded Mg-1Ca-1Zn-0.6Zr alloy, *Mater. Sci. Eng. A* 653 (2016) 27-34.
- [19] T. Homma, N. Kunito, S. Kamado, Fabrication of extraordinary high-strength magnesium alloy by hot extrusion, *Scripta. Mater.* 61 (2009) 644-647.
- [20] X.L. Hou, Z.Y. Cao, L.D. Wang, S.W. Xu, S. Kamado, L.M. Wang, Microstructure and mechanical properties of extruded Mg-8Gd-2Y-1Nd-0.3Zn-0.6Zr alloy, *Mater. Sci. Eng. A* 528 (2011) 7805-7810.
- [21] D.X. Liu, C.G. Guo, L.Q. Chai, V.R. Sherman, X.Q. Qin, Y.T. Ding, M.A. Meyers, Mechanical properties and corrosion resistance of hot extruded Mg-2.5Zn-1Ca alloy, *Mater. Sci. Eng. B* 195 (2015) 50-58.

- [22] C. Xu, M.Y. Zheng, K. Wu, E.D. Wang, G.H. Fan, S.W. Xu, S. Kamado, X.D. Liu, G.J. Wang, Influence of rolling temperature on the microstructure and mechanical properties of Mg-Gd-Y-Zn-Zr alloy sheets. *Mater. Sci. Eng. A* 559 (2013) 615-622.
- [23] Y. Zheng, Y. Li, J.H. Chen, Z.Y. Zou, Effects of tensile and compressive deformation on corrosion behaviour of a Mg-Zn alloy, *Corros. Sci.* 90 (2015) 445-450.
- [24] X.B. Zhang, Z.X. Ba, Z.X. Wang, Y.J. Xue, Microstructures and corrosion behavior of biodegradable Mg-6Gd-xZn-0.4Zr alloys with and without long period stacking ordered structure, *Corros. Sci.* 105 (2016) 68-77.
- [25] A. Oyane, H.M. Kim, T. Furuya, T. Kokubo, T. Miyazaki, T. Nakamura, Preparation and assessment of revised simulated body fluids, *J. Biomed. Mater. Res. A* 65 (2003) 188-195.
- [26] M. Ascencio, M. Pekguleryuz, S. Omanovic, An investigation of the corrosion mechanisms of WE43 Mg alloy in a modified simulated body fluid solution: The effect of electrolyte renewal, *Corros. Sci.* 91 (2015) 297-310.
- [27] Z.M. Shi, M. Liu, A. Atrens, Measurement of the corrosion rate of magnesium alloys using tafel extrapolation, *Corros. Sci.* 52 (2010) 579-588.
- [28] G. song, A. Atrens, Understanding magnesium corrosion-A framework for improved alloy performance, *Adv. Eng. Mater.* 5 (2003) 837-858.
- [29] M.C. Zhao, M. Liu, G. Song, A. Atrens, Influence of pH and chloride ion concentration on the corrosion of Mg alloy ZE41, *Corros. Sci.* 50 (2008)

3618-3718.

- [30] M.C. Zhao, M. Liu, G. Song, A. Atrens, Influence of the beta-phase morphology on the corrosion of the Mg alloy AZ91, *Corros. Sci.* 50 (2008) 1939-1953.
- [31] A. Srinivasan, Y. Huang, C.L. Mendis, C. Blawert, K.U. Kainer, N. Hort, Investigations on microstructures, mechanical and corrosion properties of Mg-Gd-Zn alloy, *Mater. Sci. Eng. A* 595 (2014) 224-234.
- [32] S. Zhang, G.Y. Yuan, C. Lu, W.J. Ding, The relationship between (Mg, Zn)₃RE phase and 14H-LPSO phase in Mg-Gd-Y-Zn-Zr alloys solidified at different cooling rates, *J. Alloys. Comp.* 509 (2011) 3515-3521.
- [33] L. Lin, P. Liang, L. Yang, L.J. Chen, Z. Liu, Y.M. Wang, Phase stability comparison by first principle calculation and experimental observation of microstructure evolution in a Mg-6Gd-2Zn(wt%) alloy, *Mater. Sci. Eng. A* 527 (2010) 2643-2648.
- [34] Y.J. Chen, Z.G. Xu, C. Smith, J. Sankar, Recent advances on the development of magnesium alloys for biodegradable implants, *Acta Biomater.* 10 (2014) 4561-4573.
- [35] J.B. Li, F. Wang, P.L. Mao, Z. Liu, Evolution of microstructure and tensile properties of extruded Mg-4Zn-Y alloy, *J. Rare Earths*, 32 (2014) 1189-1195.
- [36] W.H. Ma, Y.J. Liu, W. Wang, Y.Z. Zhang, Effects of electrolyte component in simulated body fluid on the corrosion behavior and mechanical integrity of magnesium, *Corros. Sci.* 98 (2015) 201-210.
- [37] L. Yang, E.L. Zhang, Biocorrosion behavior of magnesium alloy in different

- simulated fluids for biomedical application, *Mater. Sci. Eng. A* 29 (2009) 1691-1696.
- [38] X.B. Zhang, G.Y. Yuan, L. Mao, J.L. Niu, P.H. Fu, W.J. Ding, Effects of extrusion and heat treatment on the mechanical properties and biocorrosion behaviors of a Mg-Nd-Zn-Zr alloy, *J. Mech. Behav. Biomed. Mater.* 7 (2012) 77-86.
- [39] Y.S. Wang, M.J. Tan, J.J. Pang, Z.M. Wang, A.W.E. Jarfors, In vitro corrosion behaviors of Mg₆₇Zn₂₈Ca₅ alloy: From amorphous to crystalline, *Mater. Chem. Phys.* 134 (2012) 1079-1087.
- [40] M.I. Jamesh, G.S. Wu, Y. Zhou, D.R. Mckenzie, M.M.M. Bilek, P.K. Chu, Electrochemical corrosion behavior of biodegradable Mg-Y-RE and Mg-Zn-Zr alloys in Ringer's solution and simulated body fluid, *Corros. Sci.* 91 (2015) 160-184.
- [41] D. Mareci, G. Bolat, J. Izquierdo, C. Crimu, C. Munteanu, I. Antoniac, R.M. Souto, Electrochemical characteristics of bioresorbable binary MgCa alloy in Ringer's solution: Revealing the impact of local pH distributions during in-vitro dissolution, *Mater. Sci. Eng. A* 60 (2016) 402-410.
- [42] K. Huang, R.E. Logé, A review of dynamic recrystallization phenomena in metallic materials, *Mater. Des.* 111 (2016) 548-574.
- [43] C.J. Li, H.F. Sun, X.W. Li, J.L. Zhang, W.B. Fang, Z.Y. Tan, Microstructure, texture and mechanical properties of Mg-3.0Zn-0.2Ca alloys fabricated by extrusion at various temperatures, *J. Alloys. Comp.* 652 (2015) 122-131.
- [44] S. Vervynckt, K. Verbeken, P. Thibaux, Y. Houbaert, Recrystallization-

- precipitation interaction during austenite hot deformation of a Nb microalloyed steel, *Mater. Sci. Eng. A* 528 (2011) 5519-5528.
- [45] S.J. Hales, T.R. Mcnelley, Microstructural evolution by continuous recrystallization in a super plastic Al-Mg alloy, *Acta. Metall.* 36 (1988) 1229-1239.
- [46] D.K. Xu, L. Liu, Y.B. Xu, E.H. Han, The influence of element Y on the mechanical properties of the as-extruded Mg-Zn-Y-Zr alloys, *J. Alloys. Comp.* 426 (2006) 155-161.
- [47] H.F. Sun, C.J. Li, W.B. Fang, Evolution of microstructure and mechanical properties of Mg-3.0Zn-0.2Ca-0.5Y alloy by extrusion at various temperatures, *J. Mater. Process. Technol.* 229 (2016) 633-640.
- [48] H.Y. Yu, H.G. Yan, J.H. Chen, B. Su, Y. Zheng, Y.J. Shen, Z.J. Ma, Effects of minor Gd addition on microstructures and mechanical properties of the high strain-rate rolled Mg-Zn-Zr alloys, *J. Alloys.Comp.* 586 (2014) 757-756.
- [49] M.C. Zhao, M. Liu, G.L. Song, A. Atrens. Influence of pH and chloride ion concentration on the corrosion of Mg alloy ZE41, *Corros. Sci.* 50 (2008) 3168-3178.
- [50] Z.S. Shi, M. Liu, A. Atrens, Measurement of the corrosion rate of magnesium alloys using Tafel extrapolation, *Corros. Sci.* 52 (2010) 579-588.
- [51] W. Zhou, T. Shen, N.N. Aung, Effect of heat treatment on corrosion behaviour of magnesium alloy AZ91D in simulated body fluid, *Corros. Sci.* 52 (2010) 1035-1041.

- [52] N. Birbilis, K.D. Ralston, S. Virtanen, H.L. Fraser, C.H.J. Davies, Grain character influence on corrosion of ECAPed pure magnesium, *Corros. Eng. Sci. Technol.* 45 (2010) 224-230.
- [53] G.R. Argade, S.K. Panigrahi, R.S. Mishra, Effects of grain size on the corrosion resistance of wrought magnesium alloys containing neodymium, *Corros. Sci.* 58 (2012) 145-151.
- [54] J.S. Liao, M. Hotta, N. Yamamoto, Corrosion behavior of fine-grained AZ31B magnesium alloy, *Corros. Sci.* 61 (2012) 208-214.